

X-shooter Observations of the Gravitational Lens System CASSOWARY 5 ^{*}

Lise Christensen^{†1,2}, Sandro D’Odorico², Max Pettini^{3,4}, Vasily Belokurov³,
N. Wyn Evans³, Melinda Kellogg⁵ and Joël Vernet²

¹ Excellence Cluster Universe, Technische Universität München, Boltzmanstrasse 2, 85748 Garching, Germany

² European Southern Observatory, Karl-Schwarzschild-Strasse 2, 85748 Garching bei München, Germany

³ Institute of Astronomy, Madingley Rd, Cambridge, CB3 0HA, UK

⁴ International Centre for Radio Astronomy Research, University of Western Australia, 35 Stirling Hwy, Crawley, WA 6009, Australia

⁵ The University of Virginia’s College at Wise, 1 College Avenue, Wise, VA 24293, USA

Accepted 2010 April 15. Received 2010 March 24; in original form 2010 January 20

ABSTRACT

We confirm an eighth gravitational lens system in the CAmbridge Sloan Survey Of Wide ARcs in the skY (CASSOWARY) catalogue. Exploratory observations with the X-shooter spectrograph on the Very Large Telescope (VLT) of the European Southern Observatory (ESO) show the system CSWA 5 to consist of at least three images of a blue star-forming galaxy at $z = 1.0686$, lensed by an apparent foreground group of red galaxies one of which is at $z = 0.3877$. The lensed galaxy exhibits a rich spectrum with broad interstellar absorption lines and a wealth of nebular emission lines. Preliminary analysis of these features shows the galaxy to be young, with an age of $\sim 25\text{--}50$ Myr. With a star-formation rate of $\sim 20 M_{\odot} \text{ yr}^{-1}$, the galaxy has already assembled a stellar mass $M_{*} \sim 3 \times 10^9 M_{\odot}$ and reached half-solar metallicity. Its blue spectral energy distribution and Balmer line ratios suggest negligible internal dust extinction. A more in-depth analysis of the properties of this system is currently hampered by the lack of a viable lensing model. However, it is already clear that CSWA 5 shares many of its physical characteristics with the general population of UV-selected galaxies at redshifts $z = 1\text{--}3$, motivating further study of both the source and the foreground mass concentration responsible for the gravitational lensing.

Key words: gravitational lensing: strong – galaxies: abundances – galaxies: evolution.

1 INTRODUCTION

Galaxies at redshifts $z \gtrsim 1$ are generally too faint for their rest-frame ultraviolet (UV) spectra to be recorded with the high resolution and signal-to-noise (S/N) ratios required for an in-depth study of their most important physical properties. Consequently, our knowledge of the high redshift galaxy population is still largely based on analyses of stacked spectra which average together observations of many galaxies in order to improve the S/N ratio (e.g. Shapley et al. 2003; Vanzella et al. 2009; Weiner et al. 2009). A few exceptions are sources which, thanks to their fortuitous location behind foreground mass concentrations such as massive galaxies, or groups and clusters of galaxies, are strongly lensed so that their fluxes are significantly boosted. Observations of what has be-

come the archetypal strongly lensed galaxy, MS 1512-cB58 (cB58 for short) at $z = 2.7276$ (Pettini et al. 2000; Teplitz et al. 2000; Pettini et al. 2002; Baker et al. 2004; Siana et al. 2008), have provided clear demonstrations of the power of this technique in giving insights into the interstellar medium and stellar populations of distant galaxies with a level of detail which would otherwise be unobtainable until the next generation of 30+ m optical-infrared telescopes.

The large area of sky sampled by the Sloan Digital Sky Survey (SDSS, York et al. 2000) has allowed systematic searches for strongly lensed galaxies (e.g. Allam et al. 2007; Lin et al. 2009), with the dual interest of identifying and studying the most massive galaxies in the lensing objects, and distant galaxies in the lensed sources. The Sloan Lens ACS Survey, or SLACS,¹ targets galaxies with emission lines at more than one redshift, or redshifted nebular emission lines superimposed on the spectra of early

^{*} Based on public data from the X-shooter commissioning observations collected at the European Southern Observatory VLT/Melipal telescope, Paranal, Chile.
[†] lise.christensen@ph.tum.de

¹ <http://www.slacs.org/>

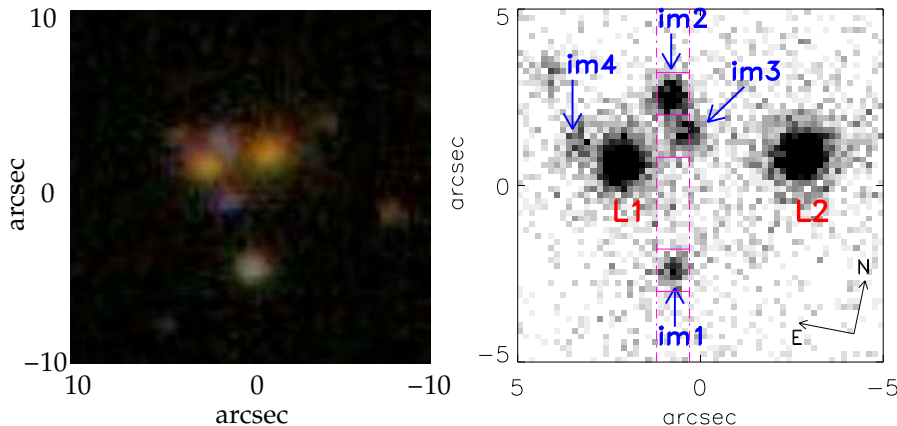


Figure 1. *Left:* 20×20 arcsec SDSS g, r, i colour composite image of the CSWA 5 system. *Right:* r' -band image of CSWA 5 recorded with a 20 s long exposure of the X-shooter acquisition and guiding camera, at position angle P.A. = 8 degrees. The scale of the right hand image is extended by a factor of two relative to the left one. In the right-hand figure, the lensed images of the source are labelled im1–im4, reflecting the sequence of light arrival times (on the assumption that im4 is one of the lensed images). Two foreground massive red galaxies are labelled L1 and L2. Note that the blue image im4 is not clearly visible in the SDSS composite on the left. The X-shooter slit is overlaid on the right-hand image of the field; we have also indicated the apertures used in the extraction of the one-dimensional spectra of im1, im2, and im3, as described in Section 2. Coordinates of all six labelled objects are given in Table 1.

Table 1. SDSS coordinates and magnitudes for the different components of the CSWA 5 lens system.

Object	RA (J2000)	Dec (J2000)	u	g	r	i	z
L1	12:44:51.35	01:06:43.0	22.34 ± 0.50	20.61 ± 0.04	19.12 ± 0.02	18.44 ± 0.02	18.02 ± 0.04
L2	12:44:51.00	01:06:44.0	22.33 ± 0.79	20.43 ± 0.06	18.44 ± 0.02	17.87 ± 0.01	17.67 ± 0.04
im1	12:44:51.22	01:06:40.1	22.07 ± 0.20	21.74 ± 0.06	22.48 ± 0.17	23.85 ± 0.67	21.75 ± 0.45
im2	12:44:51.27	01:06:45.2	20.79 ± 0.08	21.09 ± 0.04	20.91 ± 0.05	20.67 ± 0.07	20.42 ± 0.19
im3	12:44:51.23	01:06:44.2					
im4	12:44:51.44	01:06:43.5					

Notes. The magnitudes quoted are SDSS model magnitudes and are considerably more uncertain than the formal errors quoted because of blending. No SDSS magnitudes are available for images im3 and im4.

The coordinates of the objects were determined from the X-shooter acquisition image (see Figure 1), relative to the SDSS photometric source catalogue. Positional uncertainties are ~ 0.1 arcsec.

type galaxies. These candidate gravitationally lensed systems are then followed up with high spatial resolution images from the Advanced Camera for Surveys on the *Hubble Space Telescope* (*HST*; e.g. Bolton et al. 2006; Willis et al. 2005). In a complementary approach, The Cambridge Sloan Survey Of Wide ARcs in the sky (CASSOWARY) targets multiple, blue companions around massive ellipticals in the SDSS photometric catalogue as likely candidates for wide-separation gravitational lens systems (see Belokurov et al. 2009).

These and other search strategies have led to numerous recent discoveries of strongly lensed galaxies at $z \gtrsim 1$ which have been followed up in detail over a range of wavelengths (see Lemoine-Busserolle et al. 2003; Cabanac et al. 2005; Belokurov et al. 2007; Coppin et al. 2007; Swinbank et al. 2007; Cabanac et al. 2008; Stark et al. 2008; Finkelstein et al. 2009; Hainline et al. 2009; Quider et al. 2009; Siana et al. 2009; Dessauges-Zavadsky et al. 2010; Quider et al. 2010, and references therein). However, all of these studies have of necessity focused only on limited wavelength intervals, mostly in the rest-frame UV (redshifted to optical wavelengths) or the rest frame optical (redshifted into the near-infrared). It is only with the recent advent of the X-shooter spectrograph on the Very Large Telescope (VLT) facility of the European Southern Observatory (ESO), that both

wavelength ranges can now be recorded at once with good sensitivity. The obvious advantages have been demonstrated in our recent study of CASSOWARY 20 (CSWA 20, Pettini et al. 2010), a blue star-forming galaxy at $z_{\text{em}} = 1.433$ lensed into a wide separation (~ 6 arcsec) Einstein Cross by a massive luminous red galaxy at $z_{\text{abs}} = 0.741$ with velocity dispersion $\sigma_{\text{lens}} \simeq 500 \text{ km s}^{-1}$.

The current CASSOWARY catalogue² includes seven spectroscopically confirmed lensed galaxies at $z > 1$. In this paper we confirm an eighth case with X-shooter observations of CSWA 5. As can be seen from Figure 1, this multiple system consists of two foreground red galaxies one of which (L2) has an SDSS spectrum which shows it to be at $z_{\text{abs}} = 0.3877$, and four fainter sources, separated by ~ 1 –5 arcsec. Three of these images, im1, im2 and im3, are shown by the observations reported here to be gravitationally lensed images of an emission line galaxy at $z_{\text{em}} = 1.0686$, while the fourth image, not covered by our observations, remains to be confirmed spectroscopically. Coordinates and magnitudes of the different components of CSWA 5 are given in Table 1. However, we caution that the SDSS pipeline magnitudes, which are based on exponential profile fits, are likely to be significantly more uncertain than formal errors quoted, because of blending between the differ-

² <http://www.ast.cam.ac.uk/research/cassowary/>

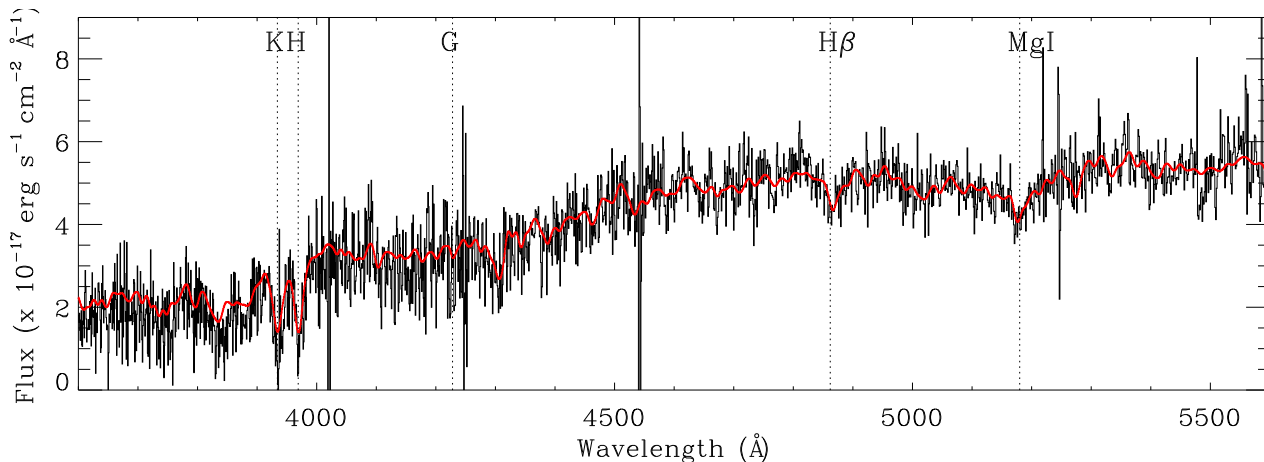


Figure 2. SDSS spectrum of galaxy L2 at $z_{\text{abs}} = 0.3877$ (shifted to the rest frame). The best fit stellar template with a velocity dispersion of $\sigma = 278 \text{ km s}^{-1}$ is shown in red.

ent components of this complex system. In particular, while image im1 may appear to be bluer than im2 from the magnitudes listed in Table 1, we suspect that this is just due to blending with the foreground red galaxy L1, because our X-shooter spectra of all three images, im1, im2, and im3, exhibit the same continuum slope.

This paper is organised as follows. We describe the X-shooter observations in Section 2 and consider the lensing galaxies in Section 3. The main focus of the paper is the rich absorption and emission line spectrum of the source, described in Sections 4 and 5 respectively. We discuss our main results in Section 6 and conclude in Section 7. Unless otherwise stated, we assume a flat cosmological model with $H_0 = 73 \text{ km s}^{-1} \text{ Mpc}^{-1}$ and $\Omega_\Lambda = 0.72$ (Spergel et al. 2007).

2 OBSERVATIONS AND DATA REDUCTION

The first of the second generation VLT instruments, X-shooter (D’Odorico et al. 2006) is a three arm, single object echelle spectrograph which was successfully integrated into standard VLT operation on October 1, 2009. The instrument covers simultaneously the wavelength range from 300 nm to 2400 nm at resolving powers $R = \lambda/\Delta\lambda = 5100, 8800$ and 5600 in the UV-B ($\Delta\lambda = 300\text{--}550 \text{ nm}$), VIS-R ($\Delta\lambda = 550\text{--}1015 \text{ nm}$), and NIR arms ($\Delta\lambda = 1025\text{--}2400 \text{ nm}$) respectively. The corresponding slit widths are 1.0, 0.9, and 0.9 arcsec respectively. Although X-shooter is optimised for observations of single targets with a 11 arcsec long slit, it also allows for simultaneous recording of close pairs of objects on the sky. As a test of the performance of the spectrograph, two CASSOWARY candidates were observed during the commissioning run of the instrument in March 2009. Results on the first object, CSWA 20, have recently been published by Pettini et al. (2010). This second paper reports the observations of CSWA 5.

Referring to Figure 1, the entrance slit of X-shooter was rotated to a position angle on the sky of P.A. = 8 degrees and aligned so as to capture the light of images im1 and im2; at this PA, part of the light from image im3 also falls into the slit. The UV-B and VIS-R detectors were binned by a factor of two in the spectral direction. The total exposure time on source was 2400 s, split into two 1200 s long integrations; each integration on source was followed by a 1200 s exposure on a nearby blank sky region. From the r' -band acquisition frame reproduced in Figure 1, we measured

a seeing full width at half maximum FWHM = $0''.9$. The seeing improved during the course of the observations; from the spatial extent of the spectra themselves we measured FWHM = $0''.8$ in the UV-B arm, $0''.7$ in the VIS-R arm, and $0''.6$ in the NIR arm. With the chosen setup, the slit losses in the three arms are estimated to be 15–10%.

The spectra were reduced with a preliminary version of the ESO X-shooter pipeline (Goldoni et al. 2006), which uses subtraction of the sky lines based on the procedures developed by Kelson (2003). For the UV-B and VIS-R data, we found it most advantageous to subtract the sky signal from the same two-dimensional (2D) frames on which the light from CSWA 5 was recorded, while for the NIR data sky subtraction from the separate blank sky 2D frames worked best. The pipeline reduction used calibration spectra taken during the commissioning run for order location and tracing, flat fielding and wavelength calibration. The final product from the pipeline is an extracted 2D, wavelength calibrated, rectified spectrum with orders combined using a weighting scheme. For further data processing and analysis we used standard IRAF tools. We produced 1D spectra using a 1.2 arcsec extraction aperture in all three arms and for all three images of the source (see right panel of Figure 1). As discussed in Section 4, the 16 strongest emission lines which were clearly detected in all three spectra were measured to be at the same redshift within $\Delta z = 5 \times 10^{-5}$. Furthermore, we found no significant differences in the emission line ratios nor in the continuum slopes of the spectra of images im1, im2 and im3, leading us to conclude that all three images are lensed counterparts of the same background galaxy. Thus, unless otherwise specified, the following analysis was performed on the sum of the spectra of im1, im2 and im3, so as to maximise the S/N ratio of the data.

Absolute flux calibration was performed with reference to the *HST* white dwarf standard GD 71, while the O8 V star Hipparcos 69892 provided a reference smooth spectrum for dividing out telluric absorption. Both stars were observed the night prior to the observations of CSWA 5. Even though Hipparcos 69892 was observed at similar airmass as CSWA 5, the correction for atmospheric absorption is not perfect, especially in the regions of low transmission between the *J*, *H*, and *K* bands. A correction for atmospheric extinction was applied assuming a standard atmospheric extinction curve. Overall, we expect the absolute flux calibration of these commissioning data to be accurate to within $\sim 20\%$, based on the

comparison between the spectrum and the SDSS magnitudes of im1 (the least contaminated of the four images).

3 FOREGROUND GALAXIES

Our X-shooter observations described above did not include either of the (presumably) foreground red galaxies visible in Figure 1. Galaxy L2 has an SDSS spectrum reproduced in Figure 2. We identify a number of stellar absorption features, labelled in Figure 2, which indicate that it lies at redshift $z_{\text{abs}} = 0.3877$. In order to obtain an estimate of the velocity dispersion (and hence the mass) of the galaxy, we used the penalised pixel fitting method of Cappellari & Emsellem (2004), taking into account the difference in velocity resolution between the input stellar template spectra of Sánchez-Blázquez et al. (2006) and the SDSS spectrum. The best fit gives a stellar velocity dispersion $\sigma_{L2} = 278 \pm 6 \text{ km s}^{-1}$, where the uncertainty reflects the dispersion in the values of σ obtained with different stellar templates. The corresponding mass is $M(r) = \pi \sigma^2 r / G$ (appropriate to an isothermal sphere), or $M_{L2} \simeq 6 \times 10^{11} M_{\odot}$, adopting $r = 10 \text{ kpc}$.

At redshift $z = 0.3877$, the SDSS z filter is closest to rest-frame r . From the SDSS measured magnitude $z(L2) = 17.67$, we deduce an absolute magnitude $M_r(L2) = -23.17$, given the distance modulus $m - M = 41.17$ in our cosmology and applying an evolutionary correction of $0.85z$ to M_r , as proposed by Bernardi et al. (2006). There is no SDSS spectrum for galaxy L1. If it is at the same redshift as L2, $z = 0.3877$, its absolute magnitude is $M_r(L1) = -22.82$ and the projected separation between the two galaxies is 28 kpc. The absolute magnitude and velocity dispersion of L2 are within the range of values found by Bernardi et al. (2006) in their sample of massive early-type galaxies selected from the SDSS database.

3.1 Lens Model

For the interpretation of many of the properties of the source, it would be advantageous to obtain estimates of the magnification factors which apply to images im1–im3. To this end, we attempted a simple modelling of the CSWA 5 system following the approach described in Pettini et al. (2010), but quickly realised that we have insufficient data at our disposal for even the simplest characterization of the lens. For the idealised case of an isolated singular isothermal sphere, the typical deflection is given by:

$$\Delta\theta = 1''.15 \left(\frac{\sigma}{200 \text{ km s}^{-1}} \right)^2 \left(\frac{D_{\text{ds}}}{D_s} \right) \quad (1)$$

where D_{ds} is the angular diameter distance between deflector and source, whilst D_s is the distance between observer and source. If galaxy L1 is: (a) the lens, and (b) at the same redshift as L2, then applying the measured $\sigma_{L2} = 278 \text{ km s}^{-1}$ (which would actually be an upper limit for L1, since L1 is fainter than L2—see Table 1) to eq. (1) would result in typical deflections of ~ 1.4 arcsec, or only about half the deflections of images im1–im4. We are thus led to one of two conclusions. Either L1 is substantially more massive than L2, as would be case if it is at a higher redshift, or L2 and other galaxies in the group significantly boost the lensing by L1. Presumably the second option is the more likely, given the proximity of L1 and L2 on the sky and their broadly similar magnitudes and colours (Table 1).

Lensing by binary galaxies has been studied by Shin & Evans (2008). From these authors' work, we find that three image mor-

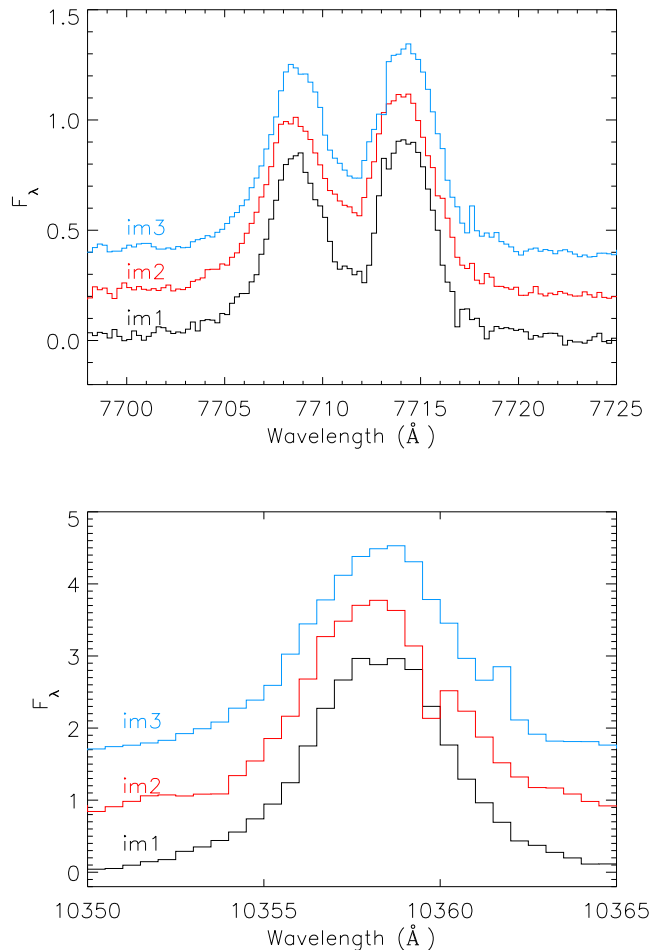


Figure 3. Profiles of the [O II] $\lambda\lambda 3728, 3730$ (upper panel) and [O III] $\lambda 5008$ (lower panel) emission lines extracted separately from images im1, im2, and im 3. The spectra have been offset vertically, and scaled to facilitate comparison. The line profiles are indistinguishable within the accuracy of the data, indicating that the three images are lensed counterparts of the same background galaxy at $z_{\text{em}} = 1.06856$.

phologies qualitatively corresponding to im1, im2 and im3 can be obtained (see lower panel of their Figure 10). However, five image morphologies qualitatively corresponding to im1, im2, im3 and im4, together with a highly demagnified fifth or central image are also possible (see middle panel of their Figure 11). Thus, in order to make progress, it will be necessary to measure the redshifts of L1 and other galaxies in the field, as well as to resolve the ambiguous status of im4. Without a satisfactory lensing model, any luminosity-dependent quantity derived for the source will be uncertain by an amount corresponding to the unknown magnification factor.

4 SOURCE GALAXY

Our X-shooter observations show images im1, im2 and im3 of the CSWA 5 system to be gravitationally lensed images of a luminous star-forming galaxy at $z = 1.0686$. This is illustrated in Figure 3, where the individual profiles of two of the best observed emission lines, the [O II] $\lambda\lambda 3728, 3730$ doublet and the [O III] $\lambda 5008$ line are shown separately for images im1, im2 and im3. The three sets of

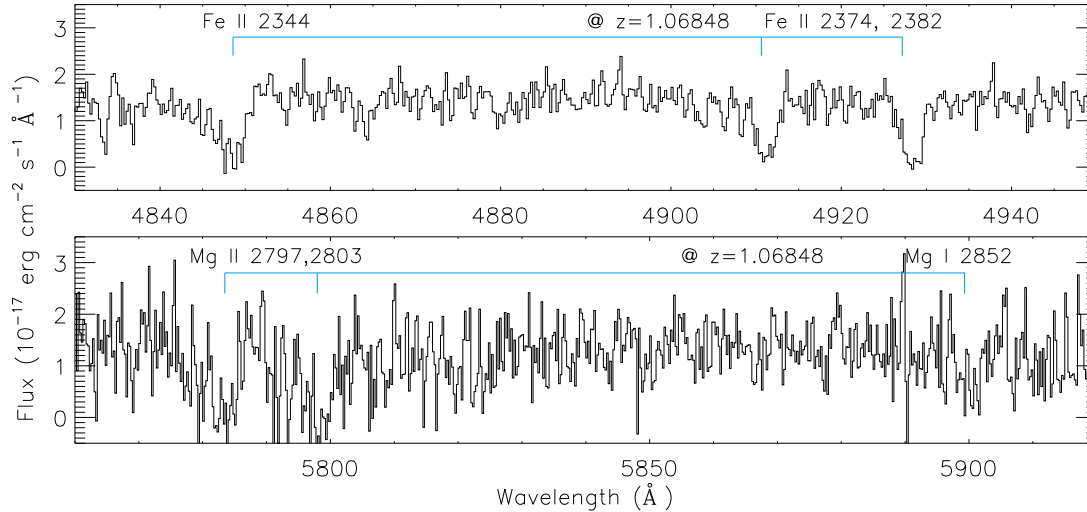


Figure 4. Examples of interstellar absorption lines in the X-shooter spectrum of CSWA 5. The full list of lines identified is given in Table 2.

Table 2. Interstellar absorption lines in the X-shooter spectrum of CSWA 5.

$\lambda_{\text{obs}}^{\text{a}}$ (Å)	Ion	$\lambda_{\text{lab}}^{\text{b}}$ (Å)	$z_{\text{abs}}^{\text{a}}$	W_0 (Å)	$\log(N/\text{cm}^{-2})$
3740.44	Si II	1808.013	1.06881	0.47 ± 0.20	14.7
3835.81	Al III	1854.520	1.06836	0.83 ± 0.27	>12.9
3853.27	Al III	1862.790	1.06855	0.61 ± 0.20	>13.2
4848.81	Fe II	2344.214	1.06842	1.54 ± 0.18	>13.8
4912.11	Fe II	2374.461	1.06873	1.07 ± 0.11	14.0
4928.75	Fe II	2382.765	1.06850	1.14 ± 0.09	>13.0
5349.78	Fe II	2586.650	1.06823	0.94 ± 0.15	>13.7
5378.10	Fe II	2600.173	1.06836	1.32 ± 0.16	>13.3
5783.56	Mg II	2796.351	1.06825	2.87 ± 0.6	>13.4
5798.96	Mg II	2803.531	1.06845	3.06 ± 0.7	>13.7
5901.91	Mg I	2852.964	1.06869	1.23 ± 0.6	>12.4

^a Vacuum heliocentric.

^b Vacuum rest wavelengths.

profiles are indistinguishable within the noise. Furthermore, when measured separately in each image, the redshifts of the 16 strongest emission lines agree to within $\Delta z = 5 \times 10^{-5}$. On the basis of this evidence, we conclude that im1, im2 and im3 are gravitationally lensed images of the same galaxy.

The galaxy exhibits a rich absorption and emission line spectrum which we now describe in detail. Unless otherwise specified, the measurements reported below refer to the *sum* of the three images, so as to maximise the S/N ratio.

4.1 Absorption Lines

The UV-B and VIS-R spectra of the source show many strong absorption lines from neutral and singly ionised species formed in the interstellar medium of the lensed galaxy. They are listed in Table 2, and a few examples are reproduced in Figure 4. They define a mean absorption redshift $z_{\text{abs}} = 1.0685 \pm 0.0002$, where the error quoted is the standard deviation from the mean. The absorption lines detected are wide, spanning a velocity range of up to $\sim 400 \text{ km s}^{-1}$.

With the relatively short exposure time devoted to CSWA 5 during the X-shooter commissioning, the signal-to-noise ratio of the spectra is low in the continuum, $S/N \simeq 5$. Thus, only the

strongest interstellar absorption lines could be detected with confidence. Such lines are saturated and unsuitable for column density determination. Under these circumstances, application of the apparent optical depth method of Savage & Sembach (1991) yields lower limits to the column densities N . Out of the transitions listed in Table 2, only two, Si II $\lambda 1898$ and Fe II $\lambda 2374$, may be sufficiently weak to provide estimates of $N(\text{Si II})$ and $N(\text{Fe II})$ respectively. Taken at face value, the column densities of these two ions may indicate a depletion of Fe by a factor of ~ 5 , since Si and Fe have comparable relative abundances in the Sun (Asplund et al. 2009), whereas $N(\text{Fe II}) \simeq 1/5 N(\text{Si II})$ in CSWA 5.

4.2 Emission Lines

Thanks to its wide wavelength coverage, the X-shooter spectrum of CSWA 5 includes a multitude of nebular emission lines, from He I $\lambda 10833$ to the C III] $\lambda\lambda 1907, 1909$ doublet; a selection is reproduced in Figure 5. As can be seen from Table 3, we detect 11 members of the Balmer series, as well as Pa δ , and several transitions of He, C, N O, Ne, S and Ar in a variety of ionisation stages. The emission lines define a mean redshift $z_{\text{em}} = 1.06856 \pm 0.00004$ (1σ), weighted by the flux in each line.

The strongest emission lines are best fit with a combination of two Gaussian functions; a narrow component centred at $z_1 = 1.06859$ with a velocity dispersion $\sigma_1 = 50 \pm 4 \text{ km s}^{-1}$ (after correction for the instrumental resolution) and a second, broader component centred at the lower redshift $z_2 = 1.06843$ with $\sigma_2 = 120 \pm 10 \text{ km s}^{-1}$. The uncertainties reflect the spread of values from acceptable fits to the line profiles. The redshift difference corresponds to a velocity separation $\Delta v = 23 \text{ km s}^{-1}$. The top left-hand panel in Figure 5 illustrates the profile decomposition for the [O II] $\lambda\lambda 3728, 3730$ doublet. The flux ratio between the narrow and broad component varies between 1.5:1 and 2:1 among different emission lines. The two emission components are not easily distinguishable in the weaker, noisier lines. Thus, in Table 3 we quote the integrated fluxes across the emission lines, which are independent of profile decomposition.

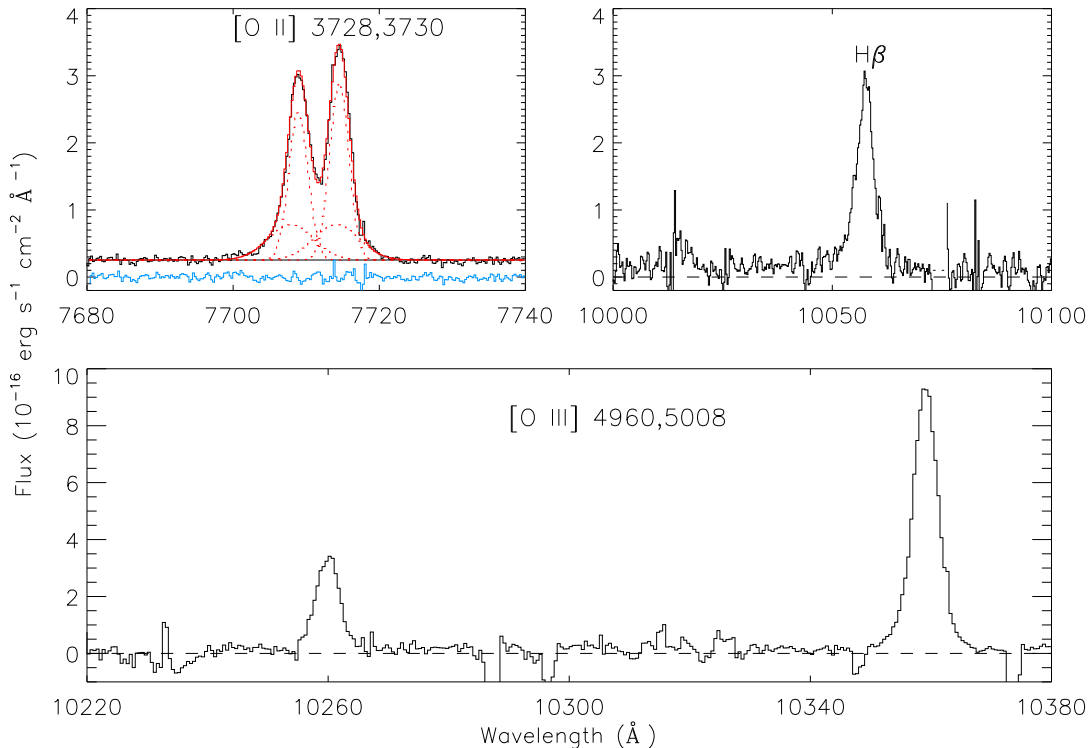


Figure 5. Examples of nebular emission lines in the X-shooter spectrum of CSWA 5. The top left-hand panel illustrates the profile decomposition into two components for the [O II] $\lambda\lambda 3728, 3730$ doublet. Black histogram: observed profile of the [O II] emission lines. Red dotted lines: individual Gaussian components; each member of the doublet is fitted with two emission components with the parameters given in Section 4.2. Red continuous line: total fitted profile to the doublet. The blue histogram near zero intensity shows the difference between the observed and fitted profiles.

5 PHYSICAL PROPERTIES

The emission line fluxes collected in Table 3 and their ratios allow us to deduce a number of physical parameters characterising the H II regions of the lensed galaxy in CSWA 5. In the following, we make the assumption that the gas is ionised by OB stars, with negligible contributions from shocks and an active galactic nucleus (AGN; see Section 6.3).

Physical quantities that are deduced from the ratios of emission lines—such as reddening, gas temperature, density, and chemical composition, or from the relative spectral energy distribution—such as the age of the stellar population, are independent of the magnification factor applicable to each of the three images covered by our observations. This is not the case, however, for quantities derived from line and continuum luminosities, such as the star formation rate (SFR) and stellar mass (M_*). In placing these quantities on an absolute scale, we are hampered not only by the lack of a lensing model (Section 3.1), but also but the unknown fraction of the light from image im3 captured by the X-shooter slit (see Figure 1). To simplify matters, we used the spectrum of image im1 alone, rather than the sum of im1, im2 and im3, in our estimates of the star formation rate (Section 5.2) and stellar mass (Section 5.5). We chose im1 because it is less affected by blending than the other images (see Figure 1), and we include explicitly the unknown magnification factor $1/f_{\text{lens}}$ in our estimates of SFR and M_* below. However, we suspect that f_{lens} may be of order unity (within a factor of 2–3) for a single image, as found by Pettini et al. (2010) for CSWA 20, which has a similar configuration to CSWA 5.

5.1 Reddening

The observed ratios of Balmer line intensities can be compared with theoretical expectations from recombination theory to deduce the amount of dust reddening. As is common practice in the analysis of H II regions, we assumed Case B recombination, an electron temperature $T_e = 10^4$ K, and electron densities in the range $n(e) = 10^2$ – 10^4 cm^{-3} (Osterbrock 1989). We did not include H α in the analysis because at $z = 1.06856$ it is redshifted to $\lambda_{\text{obs}} = 13579$ Å, between the infrared *J* and *H* bands, where atmospheric absorption is very severe and difficult to correct for accurately (which presumably explains why the observed ratio H α /H β in Table 3 is $\sim 25\%$ lower than the value H α /H $\beta = 2.86$ expected for Case B recombination). From the observed H β /H γ ratio, we deduce $E(B - V) = 0.10 \pm 0.03$, while the H β /H δ ratio gives $E(B - V) = -0.09 \pm 0.05$. The higher order Balmer lines have larger relative line flux uncertainties, so the reddening derived from higher order ratios is less certain. The weighted average is $E(B - V) = 0.03 \pm 0.02$. Thus, the H II regions of CSWA 5 (or at least the unobscured portions we see) suffer little dust reddening. Since the extinction is low ($A_V \simeq 0.1$ mag, taking the usual ratio of total to selective extinction $R_V \equiv A_V/E(B - V) \simeq 4$, Calzetti et al. 2000) and consistent with zero within the uncertainties, we did not include it in the analysis described in the following subsections.

Table 3. Nebular emission lines in the X-shooter spectrum of CSWA 5.

$\lambda_{\text{obs}}^{\text{a}}$ (Å)	Ion	$\lambda_{\text{lab}}^{\text{b}}$ (Å)	z_{em}^{a}	Flux ^c
3944.30	C III]	1906.68	1.06867	0.82±0.20
3947.92	[C III]	1908.73	1.06835	0.70±0.12
7710.59	[O II]	3728.38	1.06808	11.24±0.06
7716.01	[O II]	3730.29	1.06848	11.72±0.03
7802.38	H I (H11)	3769.56	1.06984	0.33±0.06
7858.64	[S III]	3796.72	1.06985	0.25±0.04
7858.64	H I (H10)	3796.84	...	blend
7936.00	H I (H9)	3836.47	1.06857	0.82±0.14
8005.76	[Ne III]	3869.86	1.06875	2.93±0.11
8047.27	H I (H8)	3890.15	1.06863	1.56±0.07
8047.27	He I	3889.75	1.06880	blend
8209.95	[Ne III]	3968.59	1.06873	0.61±0.17
8215.31	H I (H7)	3971.20	1.06872	1.35±0.08
8487.74	H I (Hδ)	4102.90	1.06872	2.71±0.09
8981.69	H I (Hγ)	4341.69	1.06871	5.57±0.06
9252.58	He I	4472.73	1.06867	0.46±0.17
10059.59	H I (Hβ)	4862.69	1.06873	11.34±0.12
10261.48	[O III]	4960.30	1.06872	16.84±0.27
10369.68	[O III]	5008.24	1.06873	49.53±0.45
12159.93	He I	5877.25	1.06898	1.20±0.15
13037.30	O I	6302.05	1.06874	1.77±0.37
13580.46	H I (Hα)	6564.66	1.06872	24.12±0.50
13623.41	[N II]	6585.27	1.06877	4.33±1.13
14618.95	He I	7067.14	1.06858	0.12±0.05
14765.79	[Ar III]	7137.77	1.06868	0.17±0.05
19722.90	[S III]	9533.71	1.06875	2.56±0.07
19797.52	H I (Paδ)	10052.2	1.06947	2.93±0.20
22412.11	He I	10833.3	1.06882	1.55±0.11

^a Vacuum heliocentric. The redshift errors are typically 2×10^{-5} , although in the worst cases—where a feature is contaminated by sky residuals or telluric absorption, the redshift error can be up to ten times higher.

^b Vacuum rest wavelengths.

^c Integrated line fluxes in units of $10^{-16} \text{ erg s}^{-1} \text{ cm}^{-2}$. The errors quoted reflect only the random uncertainties from the counting statistics and do not include systematic sources of error resulting from correction for atmospheric absorption, subtraction of sky emission lines, and absolute flux calibration. For some emission lines (e.g. Hα), the systematic errors can be much larger than the random errors.

5.2 Star Formation Rate

We can obtain estimates of the star formation rate from the luminosities in the Hα emission line and the near-UV continuum, using the calibrations of these measures by Kennicutt (1998). Using the Hβ flux measured for im1, $F(\text{H}\beta) = 3.1 \times 10^{-16} \text{ erg s}^{-1} \text{ cm}^{-2}$, and the unreddened Case B recombination ratio $F(\text{H}\alpha)/F(\text{H}\beta) = 2.86$, we deduce $F(\text{H}\alpha) = 8.9 \times 10^{-16} \text{ erg s}^{-1} \text{ cm}^{-2}$ and a luminosity $L(\text{H}\alpha) = 5.1 \times 10^{42} \text{ erg s}^{-1}$. This in turn implies:

$$\text{SFR} = 7.9 \times 10^{-42} L(\text{H}\alpha) \times \frac{1}{1.8} \times \frac{1}{f_{\text{lens}}} \simeq 23(M_{\odot} \text{ yr}^{-1}), \quad (2)$$

using the conversion between $L(\text{H}\alpha)$ and SFR proposed by Kennicutt (1998). The two correction factors account for: (i) the flattening of the initial mass function (IMF) below $1 M_{\odot}$ (Chabrier 2003) relative to the single power law of the Salpeter (1955) IMF assumed by Kennicutt (1998), and (ii) the unknown lensing magnification of image im1, f_{lens} , as discussed above.

Turning to the UV continuum, we measure $F = 6.1 \times 10^{-18} \text{ erg cm}^{-2} \text{ s}^{-1} \text{ \AA}^{-1}$ from our X-shooter spectrum of im1 at observed wavelengths near 5800 Å. The corresponding rest-frame

luminosity near 2800 Å, $L_{\nu}(2800) = 1.9 \times 10^{29} \text{ erg s}^{-1} \text{ Hz}^{-1}$, implies:

$$\text{SFR} = 1.4 \times 10^{-28} L_{\nu}(2800) \times \frac{1}{1.8} \times \frac{1}{f_{\text{lens}}} \simeq 15(M_{\odot} \text{ yr}^{-1}), \quad (3)$$

with the same correction factors as above. The two values of SFR are in reasonable agreement, given the systematic uncertainties affecting the two estimators, which sample different portions of the IMF (see Meurer et al. 2009).

5.3 Electron Temperature and Density

At the S/N ratio of the present data, the auroral lines most commonly used for the determination of the electron temperature, [O III] λ4363, [N II] λ5755, and [S III] λ6312 are below the detection limit. The 3σ upper limit $F(4363) \leq 0.3 \times 10^{-16} \text{ erg s}^{-1} \text{ cm}^{-2}$ translates to an upper limit on the temperature $T_e \leq 9900 \text{ K}$ (Aller 1984). Turning to density sensitive line ratios, we resolve both the [O II] λλ3728, 3730 and the C III] λλ1907, 1909 doublets, while [S II] λλ6716, 6731 falls between the *J* and the *H* bands, where the atmospheric transmission is a few percent only. We used the NEBULAR package in IRAF, incorporating the calculations by Shaw & Dufour (1995), to deduce $n(e) = 315 \pm 15 \text{ cm}^{-3}$ from the observed $F(3726)/F(3728)$ ratio, assuming $T_e = 10000 \pm 1000 \text{ K}$. Although less tightly constrained, the observed $F(1907)/F(1909)$ ratio is consistent with the electron density deduced from the higher S/N ratio [O II] doublet.

5.4 Chemical Abundances

With many nebular lines detected, we can estimate the abundances of the C, N, O group using a variety of strong emission line diagnostics. Results are collected in Table 4.

Oxygen. Oxygen is the element most commonly used to characterise the overall degree of metal enrichment of H II regions and we thus consider it first. Among the many calibrations of the oxygen abundance based on the ratios of strong emission lines (e.g. Kewley & Ellison 2008), the *R23* method first proposed by Pagel et al. (1979) is the one still most commonly applied, at least to low redshift galaxies. We used the calibration of the index $R23 \equiv [F(3728) + F(3730) + F(4960) + F(5008)]/F(\text{H}\beta)$ by Kobulnicky & Kewley (2004), appropriate to the lower branch of the double-valued *R23* vs. O/H relation, to deduce $12 + \log(\text{O}/\text{H})_{R23} = 8.28$, or approximately 40% of the oxygen abundance in the Sun (Asplund et al. 2009) and in the Orion nebula (Esteban et al. 2004). The random error in the value of $\log(\text{O}/\text{H})$ is small and negligible compared with the 0.2–0.3 dex systematic uncertainty in the calibration of the *R23* index (Kewley & Ellison 2008). The lower branch solution is favoured by the low value of the N abundance deduced below.

The calibrations of the oxygen abundance based on the ratios of nitrogen, oxygen and Balmer lines proposed by Pettini & Pagel (2004) have the advantages, compared to *R23*, of being single-valued and relatively robust to errors in flux calibration and dust extinction. However, in the case of CSWA 5, their use is possibly compromised by the awkward redshifted wavelengths of Hα and the [N II] λλ6550, 6585 doublet which fall between the *J* and *H* bands, as already explained. We deduce $12 + \log(\text{O}/\text{H})_{N2} = 8.47 \pm 0.07$ from consideration of the ratio $N2 \equiv \log[F(6585)/F(\text{H}\alpha)]$, and $12 + \log(\text{O}/\text{H})_{\text{O3N2}} =$

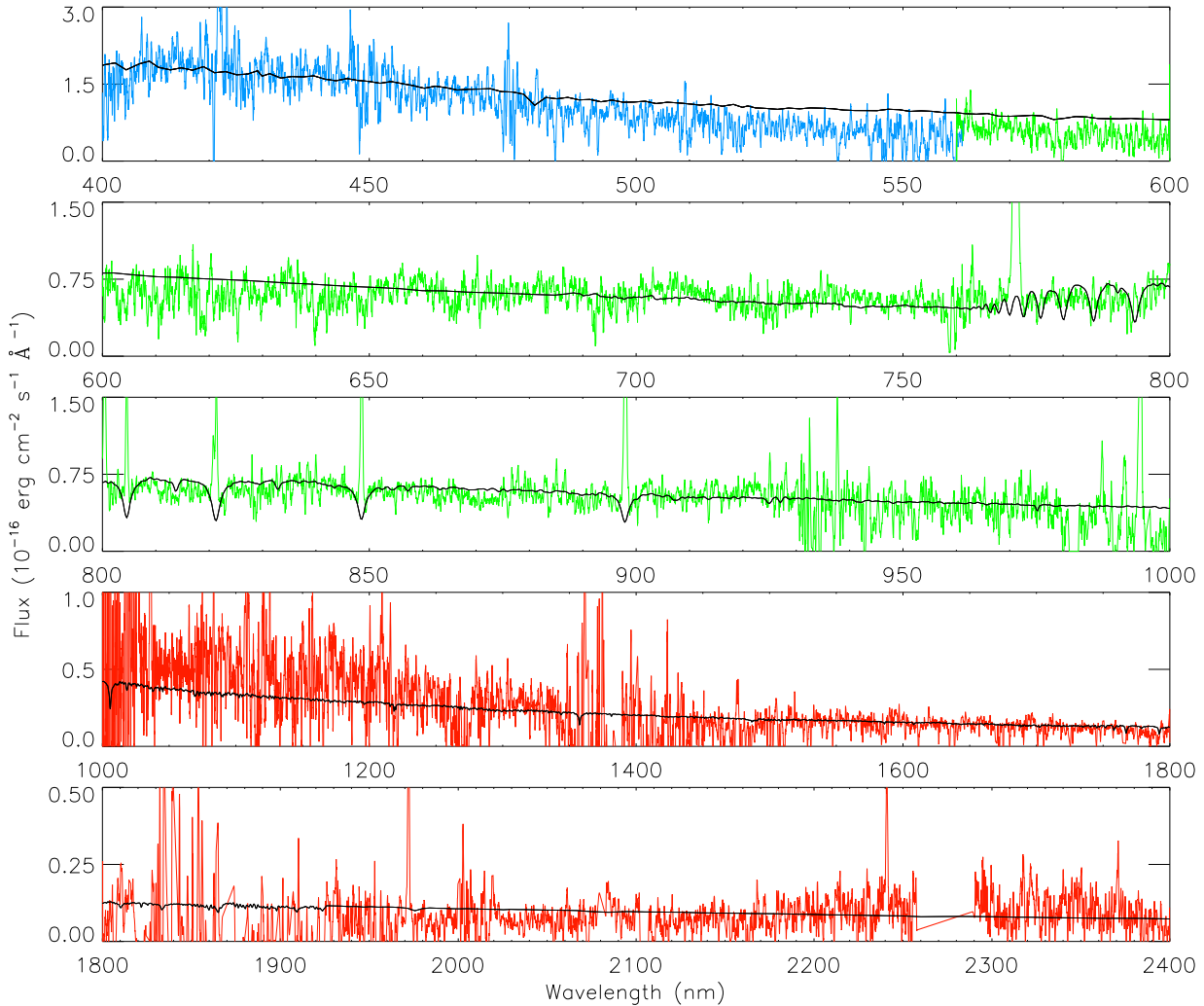


Figure 6. X-shooter spectrum of image im1 in CSWA 5, colour-coded to show the spectral ranges covered by the three arms of the spectrograph, as follows: blue is UV-B, green is VIS-R, and red is NIR. The spectrum has been smoothed with a boxcar filter of width 2.5 \AA . Overplotted in black is the best-fitting template spectrum computed with a Bruzual & Charlot (2003) model for a 40 Myr-old continuous star formation episode and assembled stellar mass $M_* = 2.8 \times 10^9 M_\odot$.

Table 4. C, N, O Abundances in CSWA 5.

$12 + \log(\text{O}/\text{H})$	$\log(\text{N}/\text{O})$	$\log(\text{C}/\text{O})$
8.3–8.5	-1.0 ± 0.1	-0.6 ± 0.2

8.29 ± 0.04 from the ratio $O3N2 \equiv \log[F(5008)/F(H\beta)] - \log[F(6585)/F(H\alpha)]$, using in both cases the calibrations of these indices deduced by Pettini & Pagel (2004). Again, the random errors quoted are small compared to the 0.2–0.3 dex systematic uncertainties of the calibrations. We conclude that the oxygen abundance in the lensed galaxy in CSWA 5 is $12 + \log(\text{O}/\text{H}) = 8.3\text{--}8.5$, or $(\text{O}/\text{H})_{\text{CSWA 5}} \simeq 0.4\text{--}0.65 (\text{O}/\text{H})_\odot$.

Nitrogen. In the absence of temperature-sensitive auroral lines, we make use of the method developed by Thurston et al. (1996) to deduce the relative abundances of N and O. These authors used photoionization models to deduce a relationship between the [N II] temperature and the $R23$ index; in our case, $t_{[\text{N II}]} = 11\,000 \pm$

1000 K. Once the [N II] temperature is known, the N/O ratio can be deduced directly from the ratio of the [N II] $\lambda\lambda 6550, 6585$ and [O II] $\lambda\lambda 3728, 3730$ doublets (Pagel et al. 1992), under the assumption that $\text{N}^+/\text{O}^+ \simeq \text{N}/\text{O}$ which Thurston et al. (1996) argue introduces only a small error. Following this procedure, we find $\log(\text{N}/\text{O})_{\text{CSWA 5}} = -0.95 \pm 0.10$ or $\sim 80\%$ of the solar value $\log(\text{N}/\text{O})_\odot = -0.86$ (Asplund et al. 2009). A slightly subsolar N/O ratio when the abundance of oxygen is ~ 0.5 solar is in line with the large body of such measurements now available in galaxies at a range of redshifts (e.g. Izotov et al. 2006; Pettini et al. 2008).

Carbon. In the low density limit, the ratio $\text{C}^{+2}/\text{O}^{+2}$ can be deduced from the measured fluxes of the C III] $\lambda\lambda 1907, 1909$ and [O III] $\lambda\lambda 4960, 5008$ doublets and a knowledge of the relevant collision strengths. Using the line emissivities given by Aller (1984), we deduce $\log(\text{C}^{+2}/\text{O}^{+2}) = -0.6 \pm 0.2$, for $T_e = 10\,000 \pm 1000 \text{ K}$. The ionization correction factor to deduce C/O from $\text{C}^{+2}/\text{O}^{+2}$ is expected to be small (Garnett et al. 1995), and therefore we find $(\text{C}/\text{O})_{\text{CSWA 5}} \simeq 0.3\text{--}0.7 (\text{C}/\text{O})_\odot$, where $\log(\text{C}/\text{O})_\odot = -0.26$ (Asplund et al. 2009). As for nitrogen, the

sub-solar C/O ratio in CSWA 5 conforms to the established behaviour of C/O vs. O/H in metal-poor H II regions (Garnett et al. 1995, 1999), Galactic stars (Akerman et al. 2004; Fabbian et al. 2009), and Lyman break galaxies (Shapley et al. 2003; Erb et al. 2010).

5.5 Age and Assembled Stellar Mass

Finally, we can obtain estimates of the age and stellar mass of the lensed galaxy by comparing its observed spectral energy distribution (SED), from the rest frame UV to the near-IR (from $\sim 2000 \text{ \AA}$ to $\sim 1.2 \mu\text{m}$ where our X-shooter spectrum has the highest S/N ratio), to those of synthetic spectra computed with simple stellar population models (e.g. Erb et al. 2006b). For this purpose, we used the population synthesis code of Bruzual & Charlot (2003) with Chabrier (2003) IMF, metallicity $Z = 0.4Z_{\odot}$ (Section 5.4), and no internal reddening (Section 5.1). We generated two families of models with these parameters, for the two limiting cases of continuous star formation and an instantaneous burst, in each case varying the age from 1 to 70 Myr. The best fitting models and the corresponding values of age and assembled stellar mass were determined by minimizing the value of χ^2 , given by:

$$\chi^2 = \sum_{\lambda} \frac{(f_{\text{obs},\lambda} - b \times f_{\text{model},\lambda})^2}{\sigma_{\text{obs},\lambda}^2} \quad (4)$$

where $f_{\text{obs},\lambda}$ and $\sigma_{\text{obs},\lambda}$ are the observed flux at wavelength λ and its error respectively, and $f_{\text{model},\lambda}$ is the flux of the Bruzual & Charlot (2003) model spectrum at the same wavelength. The normalization factor b gives the stellar mass of the galaxy.

In fitting the model spectra to the X-shooter spectrum of image im1, we excluded regions affected by strong telluric absorption or by prominent residuals in the subtraction of sky emission lines. We found that the best fitting models (see Figure 6) are those with ages of 40 ± 10 Myr and stellar masses $M_* = (2.8 \pm 1.0) \times 10^9 \times 1/f_{\text{lens}} M_{\odot}$, where f_{lens} is the unknown magnification factor of im1, and the error includes the 20% uncertainty in the absolute flux calibration (Section 2).

These values appear to be robust to the choice of star formation mode, with the single burst and continuous star formation models converging to similar solutions. We also investigated the possibility that the stellar continuum suffers a greater extinction than the H II emission lines, since the former could in principle sample a different (presumably older) stellar population than the latter. However, without recourse to the rest frame far-UV spectral range (which is inaccessible from the ground at $z = 1.0686$), we come up against the well-known age-extinction degeneracy. For example, models in which the stellar continuum is reddened with a colour excess $E(B - V) = 0.3$ also provide satisfactory fits to the X-shooter spectrum of CSWA 5, albeit with younger preferred ages of 25 ± 7 Myr and lower stellar masses of $(2.3 \pm 0.7) \times 10^9 \times 1/f_{\text{lens}} M_{\odot}$.

We can obtain an independent estimate of the age of the starburst from consideration of the equivalent width of the H β emission line, $W_0(\text{H}\beta) \simeq 100 \text{ \AA}$, using the values of $W_0(\text{H}\beta)$ as a function of time calculated with the STARBURST99 spectral synthesis code (Leitherer et al. 2001). The equivalent widths of the Balmer recombination lines fall rapidly following a burst of star formation and $W_0(\text{H}\beta) < 100 \text{ \AA}$ for all ages greater than 5 Myr. On the other hand, the time dependence is less steep for continuous star formation and ages of ~ 25 Myr are indicated, in better agreement the age inferred from the analysis of the UV to near-IR SED.

6 DISCUSSION

Summarizing our findings, we have established that CSWA 5 is an actively star-forming galaxy at $z = 1.0686$ lensed by an apparent foreground group of massive red galaxies, at least one of which is at $z = 0.3877$. The lensed source is forming stars at a rate $\text{SFR} \simeq 20 M_{\odot} \text{ yr}^{-1}$, suffers negligible reddening, has an oxygen abundance of approximately half-solar, and sub-solar N/O and C/O ratios (as expected for low metallicity galaxies). Its blue spectral energy distribution, from the rest-frame UV to the near-IR, and high H β equivalent width are indicative of a young age, only ~ 25 – 50 Myr, during which time the galaxy has assembled a stellar mass of $\sim 3 \times 10^9 M_{\odot}$. The star-formation rate and stellar mass are uncertain by an unknown magnification factor, which may be of order unity for each of the four gravitationally lensed images of CSWA 5.

These physical characteristics are broadly in line with those of the population of UV-selected galaxies at redshifts $z = 1$ – 3 (e.g. Pettini et al. 2007, and references therein), as we now discuss.

6.1 Mass-Metallicity Relation

The most relevant comparison here is with the mass-metallicity relation determined by Savaglio et al. (2005) for galaxies at a mean $\langle z \rangle \simeq 0.7$ selected from the Gemini Deep Deep Survey (GDDS) and shown in Figure 7. It must be borne in mind here that such comparisons are fraught with pitfalls for the unwary, because of systematic differences between the methods used to determine both the stellar mass and the metallicity. In this particular case, the study by Savaglio et al. (2005) should be compatible with ours, as both used a Chabrier (2003) IMF in arriving at the stellar masses and the $R23$ index for the oxygen abundance (although the reliability of the latter at apparently super-solar metallicities is questionable—see Pettini 2008).

An additional complication is the unknown magnification factor which applies to our derivation of the stellar mass. If f_{lens} in Section 5.5 is of order unity, then Figure 7 shows that CSWA 5 is somewhat metal-poor for its stellar mass, compared to GDDS galaxies at $z \sim 0.7$. Definite conclusions are difficult at this stage, given the scatter of the GDDS galaxies about the mean relation in Figure 7, and the lack of objects as metal-poor as CSWA 5 in the sample considered by Savaglio et al. (2005). Taken at face value, the offset of CSWA 5 in Figure 7 is in the same sense as the more general redshift evolution of the mass-metallicity relation proposed by Maiolino et al. (2008).

6.2 Specific Star Formation Rate

Since the lens magnification factor enters into the calculation of both SFR and M_* , the ratio of these two quantities, commonly referred to as the specific star formation rate (SSFR), should not be affected. For CSWA 5 we deduce a specific $\text{SFR} = (8.2 \pm 2.2) \times 10^{-9} \text{ yr}^{-1}$. The reciprocal of this value gives a timescale for the star formation activity of $\sim 120 \pm 45$ Myr, which is ~ 3 times higher than the age deduced in Section 5.5 from SED fitting.

In Figure 8 we compare the value of SSFR in CSWA 5 with those of UV-selected galaxies at $z \simeq 2$ from the work by Erb et al. (2006b) and of lower redshift galaxies from the VVDS survey by Lamareille et al. (2009). Clearly, CSWA 5 is more akin to the former than to the latter in its relatively high SSFR and correspondingly short star formation timescale.

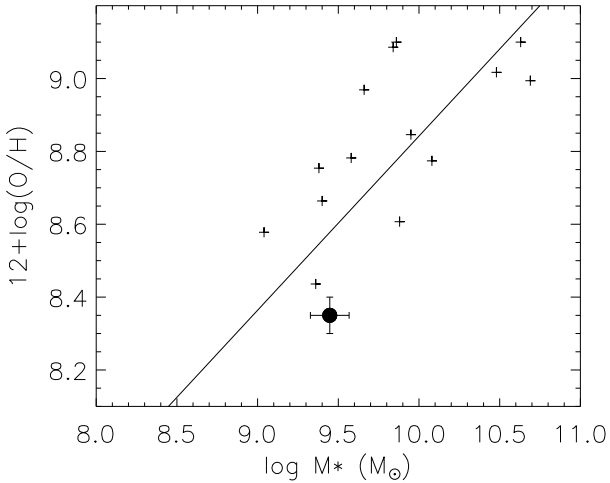


Figure 7. Mass metallicity relation for galaxies at $z \sim 0.7$ from the GDDS (crosses; Savaglio et al. 2005). The location of CSWA 5 is indicated by the large filled circle. The errors shown do not include the systematic uncertainties in the metallicity and mass determinations.

6.3 Emission line ratios

Figure 9 shows that CSWA 5 is well separated from the locus of SDSS galaxies in the ionization diagnostic diagram of Baldwin et al. (1981), sometimes referred to as the BPT diagram. While we find no evidence for the presence of an AGN in CSWA 5 from the width of the emission lines, we note that such offsets now appear to be common for the most actively star-forming galaxies (Erb et al. 2006a; Liu et al. 2008). Brinchmann et al. (2008) pointed out that, among SDSS galaxies, there is a correlation between excess SSFR and offset from the main locus occupied by ‘normal’ galaxies in the BPT diagram. Galaxies with higher SSFRs tend to exhibit higher values of the ratios $[\text{O III}]/\text{H}\beta$ and $[\text{N II}]/\text{H}\alpha$. CSWA 5 apparently fits this trend. The underlying physical explanation for the offset is not well established, but there are indications that it may be related to a higher ionization parameter of the H II regions, which in turn is presumably linked to the high star formation activity (Liu et al. 2008; Brinchmann et al. 2008).

7 CONCLUSIONS

It is encouraging and satisfying that through dedicated searches of large area surveys the number of gravitationally lensed galaxies at high redshifts continues to increase. The work presented here has not only identified a new such example in the CASSOWARY catalogue but, more importantly, has demonstrated the wealth of information on the physical conditions of these objects which can be gleaned from even relatively short exposures with the X-shooter spectrograph, thanks to its high efficiency and wide wavelength coverage. The main impediment we have found to the full characterization of CSWA 5 is the lack of a lensing model which can reproduce the deflections of the images. Higher spatial resolution imaging of the field (achievable with the *Hubble Space Telescope*) and more redshift determinations of galaxies in the field are needed for a comprehensive census of the mass distribution along the line of sight and an accurate estimate of the magnification of CSWA 5. Such information, combined with higher S/N ratio spectra of the four lensed images (the work presented in this paper is based on

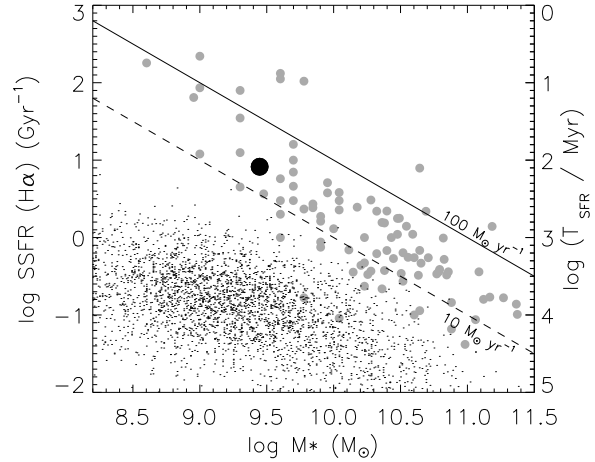


Figure 8. Specific star-formation rate of CSWA 5 (large black dot) compared with those of galaxies at $z > 2$ (grey dots; Erb et al. 2006b), and galaxies at $0 < z < 0.6$ from the VIMOS VLT Deep Survey (VVDS) (small dots; Lamareille et al. 2009). All SFRs were derived from the H α luminosities. Lines of constant SFR are indicated by the straight solid and dashed lines. The mass (but not the specific SFR) of CSWA 5 is uncertain by an unknown factor $1/f_{\text{ lens}}$ which may be of order unity. The scale on the right vertical axis shows the formation time scale (the inverse of the specific SFR).

only 40 minutes of integration on target), would lead to a full mapping of the properties of this star-forming galaxy.

As a final note, we should like to stress that the use of gravitational lensing to access the properties of galaxies at high redshifts is in some way still in its infancy. While the few cases studied so far have been very successful in providing detailed views of these systems which would otherwise have simply been unobtainable, it is also the case that nearly all of them appear to be drawn from the bright end of the galaxy luminosity function. Fainter galaxies *are* accessible with 8–10 m telescopes equipped with modern spectrographs, but are often overlooked in searches for strong gravitational lenses. By systematically extending such searches to fainter limits with current and future (e.g. with the Large Synoptic Survey Telescope) surveys, it will be possible to identify intrinsically fainter galaxies, particularly at epochs when the Universe was forming most of its stars, and thereby assemble a full picture of the galaxy formation process in action.

ACKNOWLEDGMENTS

The good quality of the spectra obtained during the commissioning runs of the instrument was the result of the dedicated and successful efforts by the entire X-shooter Consortium team. More than 60 engineers, technicians, and astronomers worked over more than five years on the project in Denmark, France, Italy, the Netherlands, and at ESO. S.D. would like to acknowledge, in representation of the whole team, the co-Principal Investigators P. Kjærgaard Rasmussen, F. Hammer, R. Pallavicini, L. Kaper, and S. Randich, and the Project Managers H. Dekker, I. Guinouard, R. Navarro, and F. Zerbi. Special thanks go to the ESO commissioning team, in particular H. Dekker, J. Lizon, R. Castillo, M. Downing, G. Finger, G. Fischer, C. Lucuix, P. Di Marcantonio, E. Mason, A. Modigliani, S. Ramsay and P. Santin. We are grateful to the anonymous referee

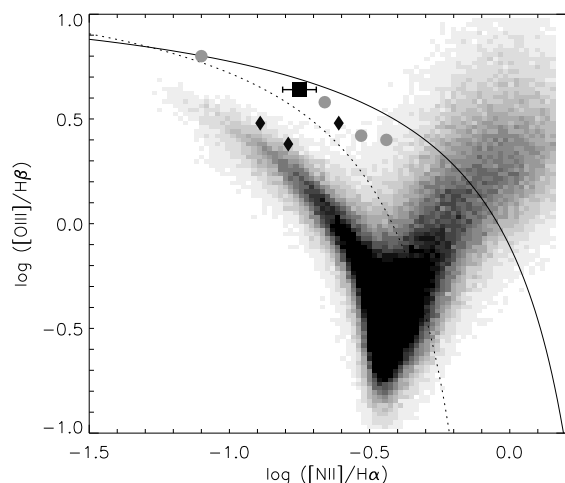


Figure 9. Emission line flux ratios of SDSS galaxies shown in grey scale (Tremonti et al. 2004). The solid and dotted lines represent the theoretical (Kewley et al. 2001) and empirical (Kauffmann et al. 2003) demarcations between star forming galaxies and galaxies harbouring AGN. Also overlaid are the values for CSWA 5 (large square), and those measured from spectra of star-forming galaxies at $z \simeq 2$ (Erb et al. 2006a, circles), and $z \simeq 1-1.4$ (Liu et al. 2008, diamonds).

for useful suggestions that improved the presentation of the work. M.P. would like to express his gratitude to the members of the International Centre for Radio Astronomy Research at the University of Western Australia for their generous hospitality during the completion of this work.

REFERENCES

- Akerman, C. J., Carigi, L., Nissen, P. E., Pettini, M., & Asplund, M. 2004, *A&A*, 414, 931
- Allam, S. S., Tucker, D. L., Lin, H., Diehl, H. T., Annis, J., Buckley-Geer, E. J., & Frieman, J. A. 2007, *ApJ*, 662, L51
- Aller, L. H., ed. 1984, *Astrophysics and Space Science Library*, Vol. 112, Physics of thermal gaseous nebulae (Dordrecht: D. Reidel)
- Asplund, M., Grevesse, N., Sauval, A. J., & Scott, P. 2009, *ARA&A*, 47, 481
- Baker, A. J., Tacconi, L. J., Genzel, R., Lehnert, M. D., & Lutz, D. 2004, *ApJ*, 604, 125
- Baldwin, J. A., Phillips, M. M., & Terlevich, R. 1981, *PASP*, 93, 5
- Belokurov, V., Evans, N. W., Hewett, P. C., Moiseev, A., McMahon, R. G., Sanchez, S. F., & King, L. J. 2009, *MNRAS*, 392, 104
- Belokurov, V., et al. 2007, *ApJ*, 671, L9
- Bernardi, M., et al. 2006, *AJ*, 131, 2018
- Bolton, A. S., Burles, S., Koopmans, L. V. E., Treu, T., & Moustakas, L. A. 2006, *ApJ*, 638, 703
- Brinchmann, J., Pettini, M., & Charlot, S. 2008, *MNRAS*, 385, 769
- Bruzual, G., & Charlot, S. 2003, *MNRAS*, 344, 1000
- Cabanac, R. A., Valls-Gabaud, D., Jaunsen, A. O., Lidman, C., & Jerjen, H. 2005, *A&A*, 436, L21
- Cabanac, R. A., Valls-Gabaud, D., & Lidman, C. 2008, *MNRAS*, 386, 2065
- Calzetti, D., Armus, L., Bohlin, R. C., Kinney, A. L., Koornneef, J., & Storchi-Bergmann, T. 2000, *ApJ*, 533, 682
- Cappellari, M., & Emsellem, E. 2004, *PASP*, 116, 138
- Chabrier, G. 2003, *PASP*, 115, 763
- Coppin, K. E. K., et al. 2007, *ApJ*, 665, 936
- Dessauges-Zavadsky, M., D’Odorico, S., Schaerer, D., Modigliani, A., Tapken, C., & Vernet, J. 2010, *A&A*, 510, A26
- D’Odorico, S., et al. 2006, in *Society of Photo-Optical Instrumentation Engineers (SPIE) Conference Series*, Vol. 6269
- Erb, D. K., Pettini, M., Shapley, A. E., Steidel, C. C., Reddy, N., & Law, D. R. 2010, *ApJ*, submitted
- Erb, D. K., Shapley, A. E., Pettini, M., Steidel, C. C., Reddy, N. A., & Adelberger, K. L. 2006a, *ApJ*, 644, 813
- Erb, D. K., Steidel, C. C., Shapley, A. E., Pettini, M., Reddy, N. A., & Adelberger, K. L. 2006b, *ApJ*, 646, 107
- Esteban, C., Peimbert, M., García-Rojas, J., Ruiz, M. T., Peimbert, A., & Rodríguez, M. 2004, *MNRAS*, 355, 229
- Fabbian, D., Nissen, P. E., Asplund, M., Pettini, M., & Akerman, C. 2009, *A&A*, 500, 1143
- Finkelstein, S. L., Papovich, C., Rudnick, G., Egami, E., LeFloc’h, E., Rieke, M. J., Rigby, J. R., & Willmer, C. N. A. 2009, *ApJ*, 700, 376
- Garnett, D. R., Shields, G. A., Peimbert, M., Torres-Peimbert, S., Skillman, E. D., Dufour, R. J., Terlevich, E., & Terlevich, R. J. 1999, *ApJ*, 513, 168
- Garnett, D. R., Skillman, E. D., Dufour, R. J., Peimbert, M., Torres-Peimbert, S., Terlevich, R., Terlevich, E., & Shields, G. A. 1995, *ApJ*, 443, 64
- Goldoni, P., Royer, F., François, P., Horrobin, M., Blanc, G., Vernet, J., Modigliani, A., & Larsen, J. 2006, in *Society of Photo-Optical Instrumentation Engineers (SPIE) Conference Series*, Vol. 6269
- Hainline, K. N., Shapley, A. E., Kornei, K. A., Pettini, M., Buckley-Geer, E., Allam, S. S., & Tucker, D. L. 2009, *ApJ*, 701, 52
- Izotov, Y. I., Stasińska, G., Meynet, G., Guseva, N. G., & Thuan, T. X. 2006, *A&A*, 448, 955
- Kauffmann, G., et al. 2003, *MNRAS*, 346, 1055
- Kelson, D. D. 2003, *PASP*, 115, 688
- Kennicutt, R. C. 1998, *ARA&A*, 36, 189
- Kewley, L. J., Dopita, M. A., Sutherland, R. S., Heisler, C. A., & Trevena, J. 2001, *ApJ*, 556, 121
- Kewley, L. J., & Ellison, S. L. 2008, *ApJ*, 681, 1183
- Kobulnicky, H. A., & Kewley, L. J. 2004, *ApJ*, 617, 240
- Lamareille, F., et al. 2009, *A&A*, 495, 53
- Leitherer, C., Leão, J. R. S., Heckman, T. M., Lennon, D. J., Pettini, M., & Robert, C. 2001, *ApJ*, 550, 724
- Lemoine-Busserolle, M., Contini, T., Pelló, R., Le Borgne, J.-F., Kneib, J.-P., & Lidman, C. 2003, *A&A*, 397, 839
- Lin, H., et al. 2009, *ApJ*, 699, 1242
- Liu, X., Shapley, A. E., Coil, A. L., Brinchmann, J., & Ma, C. 2008, *ApJ*, 678, 758
- Maiolino, R., et al. 2008, *A&A*, 488, 463
- Meurer, G. R., et al. 2009, *ApJ*, 695, 765
- Osterbrock, D. E. 1989, *Astrophysics of gaseous nebulae and active galactic nuclei* (University Science Books, Mill Valley, CA)
- Pagel, B. E. J., Edmunds, M. G., Blackwell, D. E., Chun, M. S., & Smith, G. 1979, *MNRAS*, 189, 95
- Pagel, B. E. J., Simonson, E. A., Terlevich, R. J., & Edmunds, M. G. 1992, *MNRAS*, 255, 325

- Pettini, M. 2008, in *The Metal-Rich Universe*, ed. G. Israelian & G. Meynet (Cambridge University Press), 186
- Pettini, M., et al. 2010, *MNRAS*, 402, 2335
- Pettini, M., & Pagel, B. E. J. 2004, *MNRAS*, 348, L59
- Pettini, M., Rix, S. A., Steidel, C. C., Adelberger, K. L., Hunt, M. P., & Shapley, A. E. 2002, *ApJ*, 569, 742
- Pettini, M., et al. 2007, *Nuovo Cimento B Serie*, 122, 1043
- Pettini, M., Steidel, C. C., Adelberger, K. L., Dickinson, M., & Giavalisco, M. 2000, *ApJ*, 528, 96
- Pettini, M., Zych, B. J., Steidel, C. C., & Chaffee, F. H. 2008, *MNRAS*, 385, 2011
- Quider, A. M., Pettini, M., Shapley, A. E., & Steidel, C. C. 2009, *MNRAS*, 398, 1263
- Quider, A. M., Shapley, A. E., Pettini, M., Steidel, C. C., & Stark, D. P. 2010, *MNRAS*, 402, 1467
- Salpeter, E. E. 1955, *ApJ*, 121, 161
- Sánchez-Blázquez, P., et al. 2006, *MNRAS*, 371, 703
- Savage, B. D., & Sembach, K. R. 1991, *ApJ*, 379, 245
- Savaglio, S., et al. 2005, *ApJ*, 635, 260
- Shapley, A. E., Steidel, C. C., Pettini, M., & Adelberger, K. L. 2003, *ApJ*, 588, 65
- Shaw, R. A., & Dufour, R. J. 1995, *PASP*, 107, 896
- Shin, E. M., & Evans, N. W. 2008, *MNRAS*, 390, 505
- Siana, B., et al. 2009, *ApJ*, 698, 1273
- Siana, B., Teplitz, H. I., Chary, R., Colbert, J., & Frayer, D. T. 2008, *ApJ*, 689, 59
- Spergel, D. N., et al. 2007, *ApJS*, 170, 377
- Stark, D. P., Swinbank, A. M., Ellis, R. S., Dye, S., Smail, I. R., & Richard, J. 2008, *Nature*, 455, 775
- Swinbank, A. M., Bower, R. G., Smith, G. P., Wilman, R. J., Smail, I., Ellis, R. S., Morris, S. L., & Kneib, J.-P. 2007, *MNRAS*, 376, 479
- Teplitz, H. I., et al. 2000, *ApJ*, 533, L65
- Thurston, T. R., Edmunds, M. G., & Henry, R. B. C. 1996, *MNRAS*, 283, 990
- Tremonti, C. A., et al. 2004, *ApJ*, 613, 898
- Vanzella, E., et al. 2009, *ApJ*, 695, 1163
- Weiner, B. J., et al. 2009, *ApJ*, 692, 187
- Willis, J. P., Hewett, P. C., & Warren, S. J. 2005, *MNRAS*, 363, 1369
- York, D. G., et al. 2000, *AJ*, 120, 1579